Journal of Leather Science and Engineering

RESEARCH Open Access

Homogeneous Zr and Ti co-doped SBA-15 with high specific surface area: preparation, characterization and application

Taotao Qiang[1,2*], Yajuan Xia[1,2] and Jing Zhao[1,2]

Abstract

A facile synthesis procedure is proposed to prepare homogeneous Zr and Ti co-doped SBA-15 (Zr-Ti-SBA-15) with high specific surface area of 876.0 $m^2 g^{-1}$. Based on "masking mechanism" from tanning, lactic acid was used as masking agent to obtain the uniform distribution of Zr and Ti species in the SBA-15 framework. The obtained materials were characterized by powder X-ray diffraction (XRD), nitrogen adsorption-desorption isotherms, scanning electron microscope (SEM), transmission electron microscope (TEM) and X-ray photoelectron (XPS). The results reveal that in mesoporous materials, the presence of lactic acid gives rise to the uniform distribution of Zr and Ti species. The adsorption equilibrium and kinetic studies of Zr-Ti-SBA-15 materials show that the adsorption process conforms to the Langmuir isotherm and pseudo-second-order kinetic model, respectively. Regenerational experiments show that the Zr-Ti-SBA-15 displays a significant adsorption ability for methylene blue (MB) (up to 291.6 mg/g), along with good reusability, indicating promising potentials of commercialization. Methodologically, this work provides a wide range of possibilities for further development of SBA-15 based on bimetallic and sewage disposal.

Keywords: Direct synthesis method, Zr-Ti-SBA-15, Adsorption, High specific surface area

1 Introduction

With the rapid development of industrialization, organic dyes as a serious water pollutant are applied in various industries including textiles, leather, paper-making, pigments and cosmetics [1, 2], statistically with more than 7×10^5 tons of dyes produced annually around the world, about 12% of which are lost during the processing process and approximately 20% of which are discharged with effluent. Generally speaking, the water coloration will be observed even when the dye concentration is lower than 1 ppm [3–5] and it is well-known that the presence of dyes in waste water has a negative effect on aquatic environment and also causes a serious health risks to human beings and animals [6], the total or partial removal of organic dyes which is vital for the treatment of effluent. Various techniques for the removal of dyes have been developed, including electrooxidation, ozonation, ion exchange, microbial degradation, photocatalytic degradation, etc [7], compared with which, adsorption technique has attracted extensive investigation due to its low consumption of energy, simple operation, low cost as well as the universality for diverse dyes [8].

Recently, porous nanostructured materials as adsorbent of organic dyes have been one of the most extensively studied materials owing to its large surface and abundant active sites [9], of which SBA-15 materials as a typical representative representing suitable support exhibit well-aligned nanochannels, high surface area, large pore diameter and excellent thermal stability [10], with its modification by metal atoms, including Zr [11], Ti [12], Al [13], Fe [14], widely reported in the adsorption and catalytic fields, and particularly investigations to Ti-SBA-15 used for effective removal of organic dyes from a system attracting more attentions of reaesrchers [15]. Zhang and his group [16] prepared a series of Ti-containing SBA-15 samples in the self-generated acidic condition with catalytic tests indicating that Ti-SBA-15 showed much higher photodegradation ability towards RhB than pure TiO_2 and the work from Swapan K. Das et al. [17] showed that

* Correspondence: qiangtt515@163.com
[1]College of Bioresources and Materials Engineering, Shaanxi University of Science & Technology, Xi'an, Shaanxi 710021, People's Republic of China
[2]National Demonstration Center for Experimental Light Chemistry Engineering Education, Shaanxi University of Science & Technology, Xi'an, Shaanxi 710021, People's Republic of China

synthesized Ti-SBA-15 with higher surface area than that of pure SBA-15, possessed larger H_2 uptake at higher external pressure and excellent efficiency in photocatalytic degradation of methylene blue, which indicate that the introduction of heteroatoms in SBA-15 materials is a promising approach to enhance the SBA-15 properties.

Compared to monometallic mesoporous materials, the incorporation of multi-heteroatoms into mesoporous SBA-15 framework could create new active sites and show better performance of activity and stability [18, 19]. Although much progress has been made in synthesizing bimetallic Ti-based mesoporous materials, research to Zr support on Ti-SBA-15 materials [15, 17, 20] has been rare, exemplified by a series of novel multifunctionalized Zr-Ti-SBA-15 ionic liquid filled ordered channels have been synthesized by post-grafting [21], contrasted by findings that the specific surface area of SBA-15 strongly decreases after introduction of titanium and zirconium atoms into its framework. Zr-Ti-SBA-15 synthesized via hydrothermal method has also been reported by K. Chandra Mouli et al. [22], by comparing the hydrodenitrogenation (HDN) and hydrodesulphurization (HDS) conversion of Zr-Ti-SBA-15 coming to the conclusion that the increase in HDN conversion is mainly attributable to the incorporation of Zr and Ti in the framework, while the decrease in HDS conversion originates from the poor dispersion of metal on the supports. Therefore, preparing a bimetallic mesoporous material with uniform distribution via a simple method is rational and quite necessary to modify the specific properties of mesoporous material, incorporating heteroatoms into which is through direct synthesis and post synthesis methods, with the former more relatively convenient and controllable than the latter [23].

In this work, a combination of the "masking mechanism" from tanning and the use of lactic acid as masking agent is used to synthesize a homogenous Zr and Ti co-doped SBA-15, with characterization results showing that the incorporation of lactic acid endows the even distribution of Zr and Ti in the SBA-15 framework, and no metal oxides are observed in Zr-Ti-SBA-15 samples. The mesostructure and morphology of the sample is characterized by XRD, N_2 adsorption-desorption isotherm, TEM and SEM, and the surface chemical environment is analyzed via XPS and EDS mapping. MB adsorption on Zr-Ti-SBA-15 materials and the reusability of Zr-Ti-SBA-15 are studied as well.

2 Experimental section

2.1 Materials

The structure-directing agent of triblock copolymer P123 (M = 5800) was provided by Aladdin reagent. Ethyl tetrasilicate (TEOS) ($C_8H_{20}O_4Si \geq 98.0\%$) and lactic acid ($CH_3CH(OH)$ COOH 85.0 ~ 90.0%) were used as the silicon source and masking agent, respectively. These chemicals along with sodium chloride (NaCl ≥99.5%) were purchased from Tianjin Hengxing Chemical Co., Ltd. Zirconium sulfate ($Zr(SO_4)_2{\cdot}4H_2O \geq 98.0\%$), and titanium sulfate ($Ti(SO_4)_2$) acted as zirconium and titanium source, respectively, were obtained from Tianjin Guangfu Fine Chemicals. Methylene blue ($C_{16}H_{18}ClN_3S{\cdot}3H_2O \geq 98.5\%$, M = 373.90) was supplied by Tianjin Tianli Chemical Reagent Co., Ltd. All experimental chemicals were used without being further purified.

2.2 Preparation of Zr-Ti -SBA-15

In a typical synthesis, 2 g of Pluronic 123 and 1.18 g of sodium chloride were dissolved in deionized water (60 mL) with stirring at 40 °C, and subsequently 4.5 mL of tetraethylorthosilicate (TEOS) was added dropwise and prehydrolyzed for 4 h. Next, lactic acid (the molar ratio of masking agent and zirconium sulfate was 32:1) was dissolved in a solution containing zirconium sulfate (1.44 g) and titanium sulfate (0.96 g), with clear solution obtained after stirring for a few hours. After this, the so-formed solution was added to the prehydrolyzed solution and kept stirring at the same temperature for 24 h. Then the hydrolysis was allowed to continue for another 24 h at 40 °C. After hydrolysis, the solution was transferred into an autoclave with a polytetrafluoroethylene liner and then placed in an oven for 24 h at 90 °C for a hydrostatic reaction. After the reaction, the product was filtered, washed with deionized water, and dried in an oven at 50 °C. Eventually, the dried product was calcined in air at 250 °C, 500 °C and 600 °C for 3, 3 and 1 h, respectively. Besides, a control samples was also prepared without adding any masking agent, denoted as Zr-Ti-SBA-15-C_0 (seen in Fig. 1).

2.3 Characterization of Zr-Ti-SBA-15

X-ray diffraction (XRD) patterns were obtained on a D8 Advance (Bruker) powder diffractometer with Cu-Kα radiation (λ = 0.154 nm). The wide-angle XRD patterns were carried out over a 5° ~ 80° 2θ range using a step size of 0.02° with the counting time of 0.1 s per step and low-angle XRD scans were performed at scanning velocity of 0.005 deg. s^{-1} over a 2θ range from 0.5° to 5°.

The textural properties including specific surface area (S_{BET}), pore diameter (D_{BJH}) and pore volume (V_{BJH}) of samples were evaluated from the N_2 adsorption-desorption experiment, before which the sample was degassed at 200 °C for 4 h under vacuum (10^{-3} Torr). The specific surface area was obtained from the adsorption branch using a multipoint Brunauer-Emmett-Teller (BET) method in the relative pressure ranging from 0.05 to 0.30. The pore size distribution was estimated from the N_2 desorption isotherm using the Barrett-Joyner-Halenda (BJH) model.

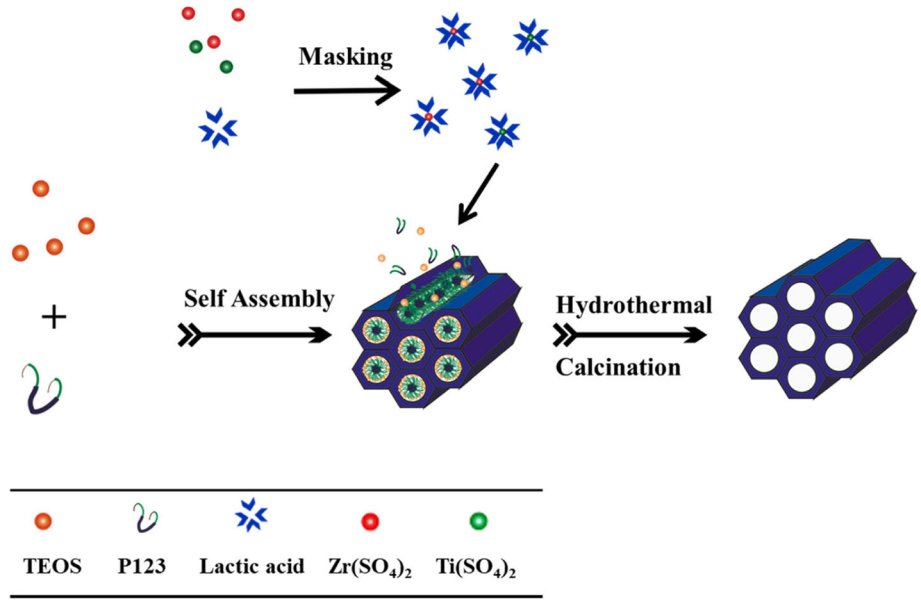

Fig. 1 Schematic illustration of synthesis process of Zr-Ti-SBA-15

The morphology of the pore structure of the Zr-Ti-SBA-15 sample was visually characterized via transmission electron microscope (TEM) on FEI Tecnai G2 F20 S-TWINFEI. Before the measurement, samples were ultrasonically dispersed in ethanol and a drop of the suspension was deposited on the carbon-coated copper mesh. Energy disperse spectroscopy mapping (EDS mapping) was performed on a FEI Tecnai G2 F20 S-TWINFEI instrument at an accelerating voltage of 20 KV to measure the elemental composition and distribution of Zr-Ti-SBA-15. Scanning electron microscopy (SEM) on a FEI Verious 460 was used to examine the surface morphology of synthesized Zr-Ti-SBA-15 samples.

The chemical states of the elements were detected by X-ray photoelectron spectroscopy (XPS), which were recorded on AXIS SUPRA. The monochromatic Al Kα radiation X-ray source (hν = 1486 eV) and Ar were used as ion source. The value of binding energy was corrected using C1s peak (284.6 eV), and the deconvolution of the obtained XPS spectral curve was analyzed via Casa XPS program.

Inductively coupled plasma atom emission spectroscopy (ICP/AES) was carried out to analyze the leaching

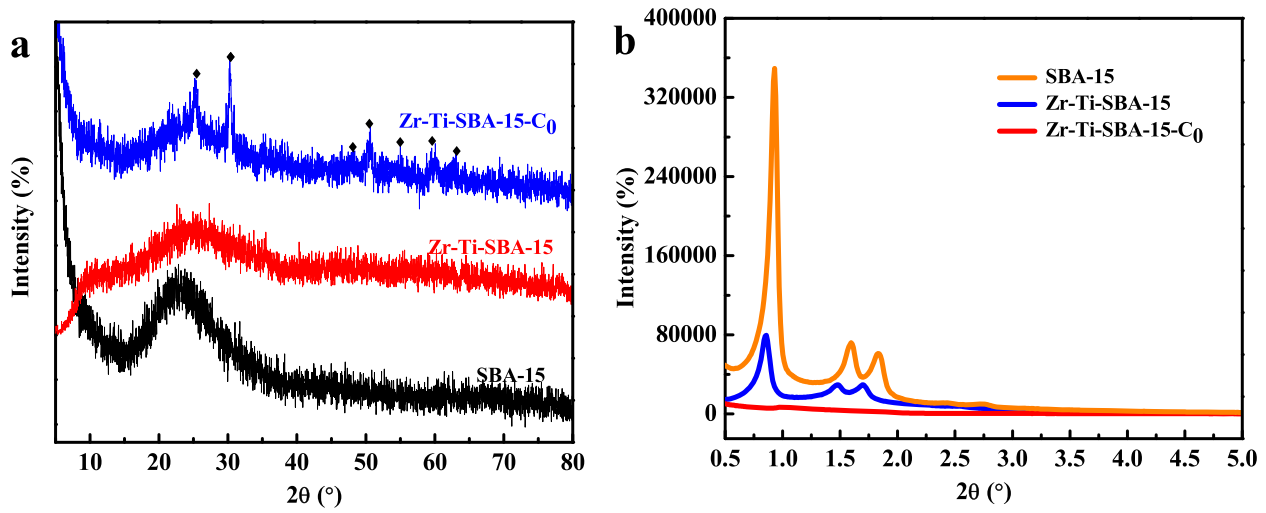

Fig. 2 XRD patterns **a** wide-angle, **b** low-angle

Table 1 XRD texture properties of the samples

Sample	d_{100}/(nm)	a_0/(nm)	D/(nm)	σ/(nm)
SBA-15	9.5	10.97	6.5	4.47
Zr-Ti-SBA-15	10.2	11.78	6.2	5.58
Zr-Ti-SBA-15-C_0	–	–	6.0	–

The value of d was obtained by Bragg equation ($2d\sin\theta = \lambda$); a_0 is the unit cell parameter ($a_0 = 2d(100)/\sqrt{3}$); D is mesopore diameter and σ is pore wall thickness ($\sigma = a_0$-D)

Table 2 Textural parameters of the samples

Sample	S_{BET}($m^2\ g^{-1}$)	D_{BJH} (nm)	V_{BJH} ($cm^3\ g^{-1}$)
SBA-15	742	6.5	0.82
Zr-Ti-SBA-15	876	6.2	0.90
Zr-Ti-SBA-15-C_0	766	6.0	0.71

of metal elements in the filtrate during desorption process. The data was detected on a IRIS Intrepid 2 Inductively Coupled Plasma-Atomic Emission Spectrometer, and filtrates were dissolved in the concentrated nitric acid solution prior to test.

2.4 Adsorption measurement

In order to detect the adsorption capacity of Zr-Ti-SBA-15, a concentration of 10, 30, 50, 70 and 90 mg/L of MB solution was prepared, and 50 mg of Zr-Ti-SBA-15 was added to the above solution. Under suitable conditions, all solution samples were shaken in a thermostat oscillator at 160 rpm to ensure effective mass transfer during adsorption process. After adsorption equilibrium, the sample was centrifuged for 5 min at a rate of 4000 rpm and its supernatant was taken. The absorbance intensity of each solution was measured by a UV−vis spectrophotometer (UV-1700, Shimadzu Scientific Instrument Inc., Japan) at a wavelength of 664 nm. The standard curve obtained by concentration and absorbance was applied to calculate the concentration of MB. The adsorption process was analyzed by adsorption kinetics and adsorption thermodynamics.

2.5 Regeneration experiment

The regeneration ability of Zr-Ti-SBA-15 was evaluated by hydrochloric acid (0.01 mol L^{-1}) as eluent. The prepared Zr-Ti-SBA-15 samples were reused for adsorption-desorption cycles, reusability of which is determined by application of the MB removal and the filtrates were collected to identify the metal concentration during the desorption process.

3 Results and discussion

3.1 XRD characterization

The X-ray diffraction pattern of all samples is depicted in Fig. 2a-b. In the wide-angle pattern (Fig. 2a), all samples exhibit a broad diffraction peaks at $2\theta = 20° \sim 30°$ which is assigned to the amorphous silica framework [24]. A serious of peaks around $2\theta = 30°$, 50°, 60°, 25°, 48°, 55° and 62° corresponding to pure ZrO_2 and TiO_2 crystal, is observed on Zr-Ti-SBA-15-C_0, but no distinct diffraction peak is found in Zr-Ti-SBA-15, implying that there is no crystallized ZrO_2 and TiO_2 formed in the Zr-Ti-SBA-15 sample, which may be contributed to the excellent masking ability of lactic acid for zirconium sulfate and titanium sulfate, leading to a lower hydrolysis rate of zirconium sulfate and titanium sulfate.

The low-angle XRD patterns of SBA-15, Zr-Ti-SBA-15-C_0 and Zr-Ti-SBA-15 are shown in Fig. 2b. For SBA-

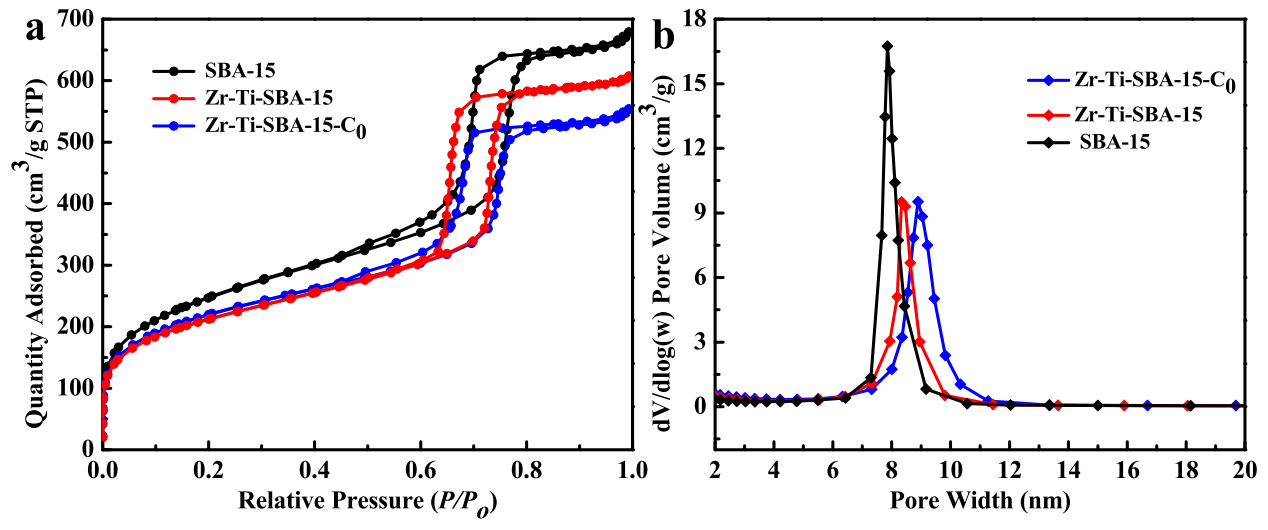

Fig. 3 N_2 adsorption-desorption isotherm (**a**) and pore size distributions (**b**)

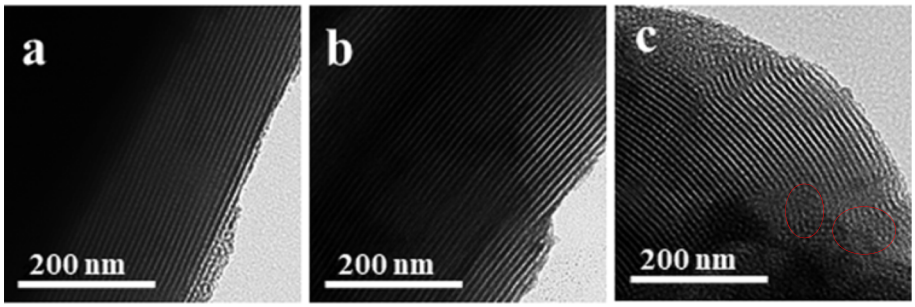

Fig. 4 TEM images **a** SBA-15, **b** Zr-Ti-SBA-15, **c** Zr-Ti-SBA-15-C_0

15 and Zr-Ti-SBA-15 samples, three well-resolved characteristic diffraction peaks centered at 0.9°, 1.5° and 1.7° can be obviously observed, corresponding to (100), (110) and (200) planes, respectively, which are typical diffraction peaks of the mesoporous material (SBA-15). This reveals that the incorporation of zirconium and titanium doesn't disturb the long rang order of SBA-15 [25]. Furthermore, there are no evident peaks in Zr-Ti-SBA-15-C_0, which may be due to the formation of titanium dioxide and zirconia partly destroyed the ordered structure of the SBA-15 [26], visually proved by TEM images (Fig. 4) visually. The XRD texture properties of Zr-Ti-SBA-15 are displayed in Table 1. As it can be seen that both of the lattice spacing and wall thickness increase when the heteroatoms are doped, suggesting that Zr and Ti atoms have successfully incorporated into silica framework.

3.2 N_2 adsorption-desorption

The adsorption-desorption isotherms of the all samples were recorded using nitrogen as the carrier gas and shown in Fig. 3a. According to the IUPAC classification, a standard type IV classification of mesoporous materials is exhibited for both samples [27]. Additionally, a sharp inflection appears at a relative pressure of 0.6–0.8 P/P_0, demonstrating the uniform pores of the N_2 capillary condensation. Furthermore, the isotherms of all the samples display H1 hysteresis loops type, suggesting the mesoporosity existence for the samples [28], which is consistent with the corresponding pore size distribution plots (as depicted in Fig. 3b). However, the branch of H1 hysteresis loop for Zr-Ti-SBA-15 is parallel and almost vertical against the abscissa, revealing that Zr-Ti-SBA-15 possesses highly pore structure. The textural properties of all samples including specific surface area, pore

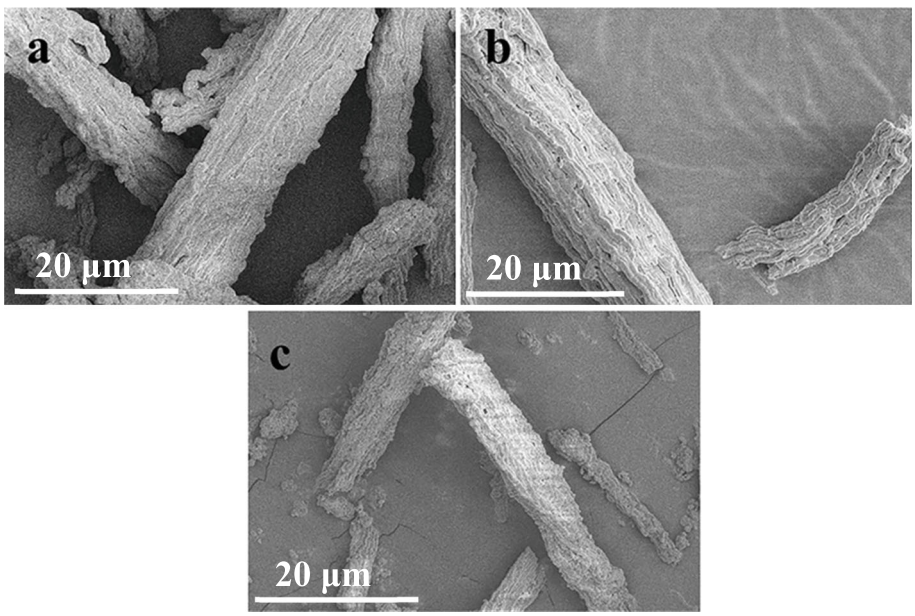

Fig. 5 SEM images **a** SBA-15, **b** Zr-Ti-SBA-15, **c** Zr-Ti-SBA-15-C_0

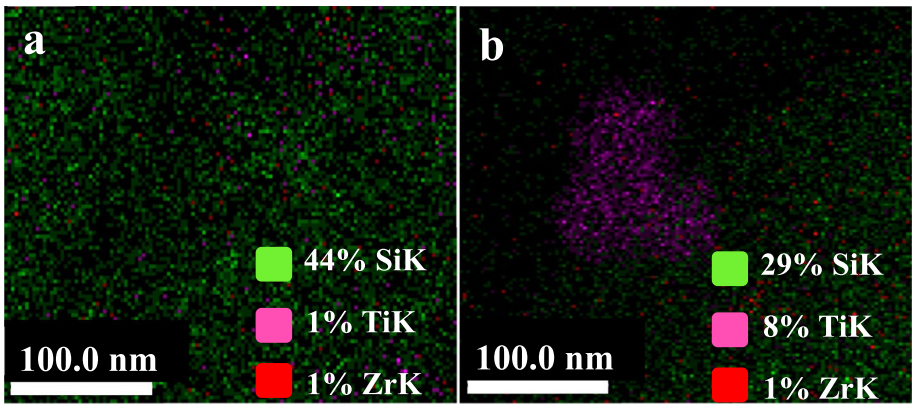

Fig. 6 EDS-mapping images **a** Zr-Ti-SBA-15, **b** Zr-Ti-SBA-15-C_0

diameter and pore volume were calculated and summarized in Table 2. It can be seen that the Zr-Ti-SBA-15 samples possess higher surface area than those of the SBA-15 and Zr-Ti-SBA-15-C_0, which could be concluded that as-synthesized materials might provide a larger contact area (i.e. many active sites) to enhance the adsorption or catalysis ability [29].

3.3 TEM and SEM characterization

The pore channel morphology of all samples was displayed visually by TEM images and the results were presented in Fig. 4. The well-ordered pore array and hexagonal structure are obviously observed in SBA-15 and Zr-Ti-SBA-15 samples. However, some black bulky dots can be seen in Zr-Ti-SBA-15-C_0, which are probably attributed to the formation of metal oxide particles [30]. Above results are well matched with those obtained from XRD and N_2 adsorption-desorption measurements.

SEM (Fig. 5) reveals that the morphology of Zr-Ti-SBA-15 is similar to that of SBA-15, which is composed of many "rope-like" domains with relatively uniform sizes of ~ 1 um and further aggregates into "wheat-like" macrostructures, indicating that the original shape of SBA-15 is reserved in Zr-Ti-SBA-15 [31, 32]. On the contrary, the morphology of Zr-Ti-SBA-15-C_0 is partly distorted, which is mainly attributed to the uneven distribution of Zr and Ti. This inference was also evidenced from EDS analysis that will be discussed later.

3.4 EDS characterization

To get a better insight into the distribution situation of heteroatoms in the Zr-Ti-SBA-15 and Zr-Ti-SBA-

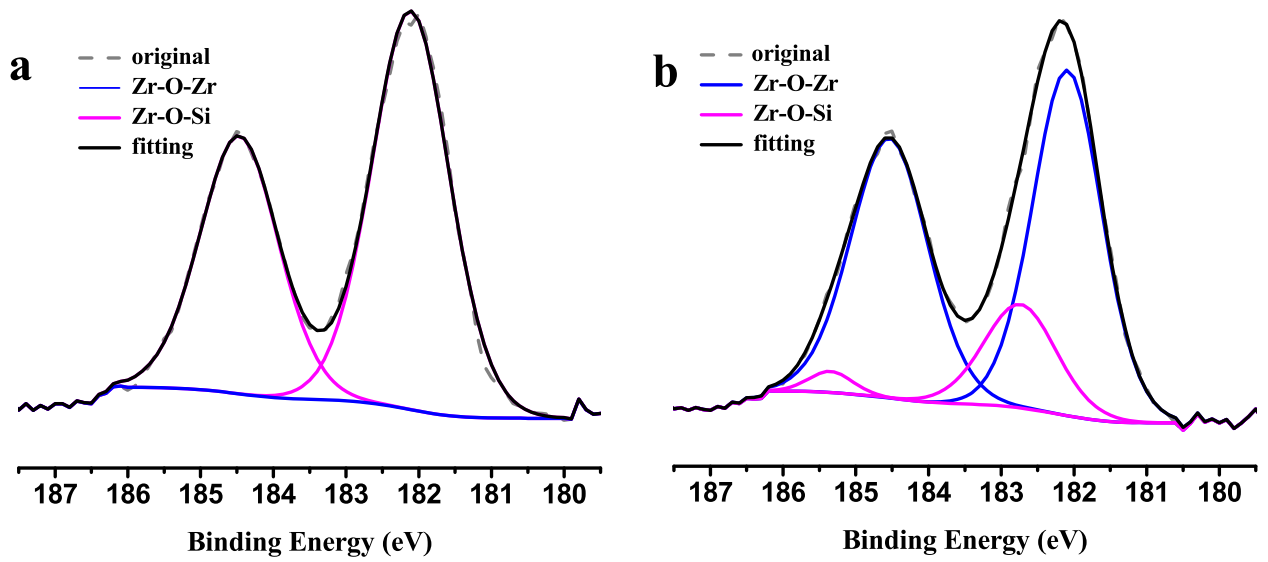

Fig. 7 XPS spectra of the samples in the Zr 3d region **a** Zr-Ti-SBA-15, **b** Zr-Ti-SBA-15-C_0

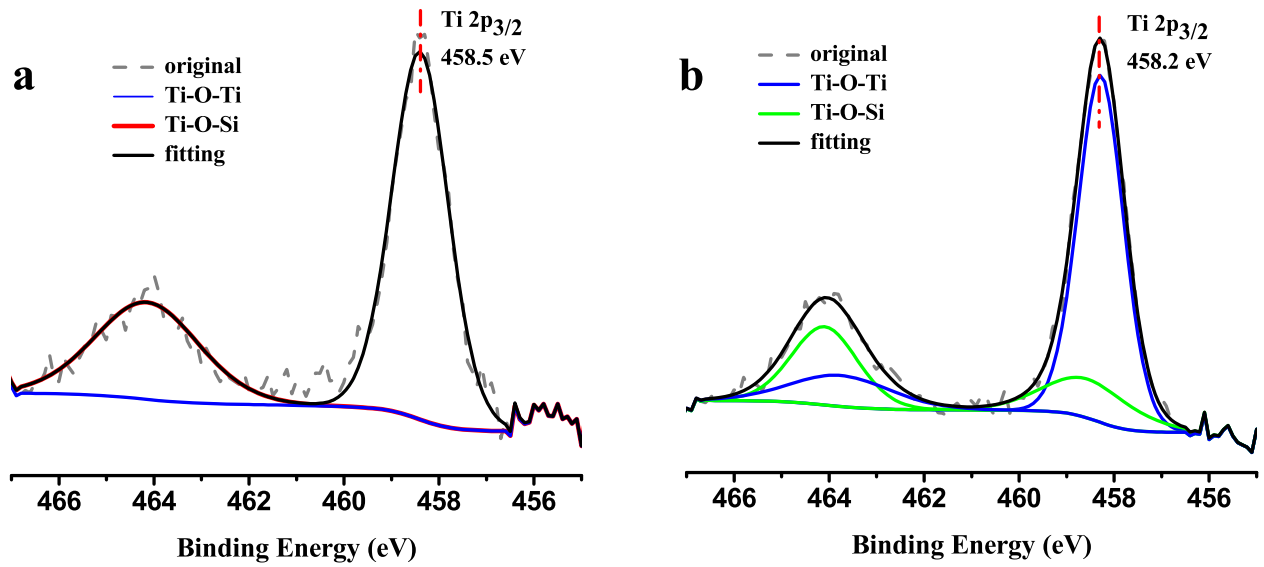

Fig. 8 XPS spectra of the samples in the Ti 2p region **a** Zr-Ti-SBA-15, **b** Zr-Ti-SBA-15-C_0

15-C_0, EDS mapping was performed with above samples. As shown in Fig. 6, the dispersion of Zr and Ti is homogenous and no phase separation is observed in the case of Zr-Ti-SBA-15 rather than Zr-Ti-SBA-15-C_0. Whereas, the uneven distribution without masking agent is caused by rapid hydrolysis of zirconium sulfate and titanium sulfate [31]. EDS analysis result indicates that Zr and Ti atoms are successfully incorporated into SBA-15 framework, and also confirms that lactic acid plays an important role in synthesizing uniform distribution of metal ions, which is consistent with SEM results.

3.5 XPS characterization

The different environments of zirconium and titanium species onto Zr-Ti-SBA-15 and Zr-Ti-SBA-15-C_0 were determined by XPS measurement. The high-resolution XPS spectra of Zr 3d are presented in Fig. 7. According to literature, the binding energies of Zr $3d_{3/2}$ and Zr $3d_{5/2}$ for bulk ZrO_2 are around 182.4 eV and 185.3 eV. Compared with Fig. 7b, the Zr-O-Si line is presented in Zr 3d spectra of Zr-Ti-SBA-15, demonstrating that Zr has successfully incorporated into SBA-15 silica framework [33]. In addition, the Zr 3d spectra of Zr-Ti-SBA-15 clearly shows doublets appearing around

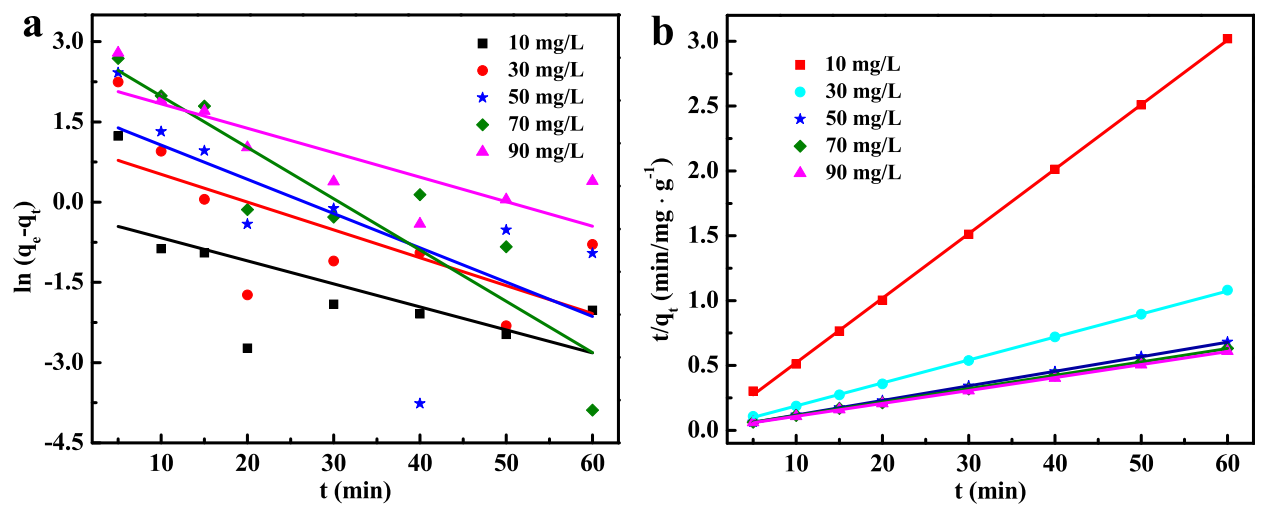

Fig. 9 Adsorption kinetics model of MB on Zr-Ti-SBA-15 **a** pseudo-first-order, **b** pseudo-second-order

Table 3 The pseudo-first-order and pseudo-second-order kinetic model parameters for MB adsorption on Zr-Ti-SBA-15 composite

Concentration	Pseudo-first-order equation			Pseudo-second-order equation		
	k_1 (min^{-1})	$q_{e,cal}$ (mg/g)	R^2	k_2 (g/mg·min)	$q_{e,cal}$ (mg/g)	R^2
10 mg/L	0.04304	0.7891	0.35043	0.1035	20.10	0.99976
30 mg/L	0.05207	2.837	0.39667	0.03265	56.34	0.99976
50 mg/L	0.06405	5.518	0.38105	0.02156	89.13	0.99991
70 mg/L	0.09596	18.96	0.81099	0.01096	96.62	0.99983
90 mg/L	0.04574	9.937	0.65239	0.01283	100.30	0.99883

185.7 eV and 183.2 eV, which is assigned to Zr $3d_{3/2}$ and Zr $3d_{5/2}$, respectively. The shift to higher binding energy for Zr 3d in Zr-Ti-SBA-15 samples could be on account of the formation of Zr-O-Si bond because of the higher electronegativity of the Si atom than that of the Zr atom. Based on above results, it is proposed that the Zr species could be in the silica framework rather than in bulk ZrO_2 [34, 35].

To profoundly discuss the environment of titanium in samples, the deconvolution of XPS spectra of Ti 2p was further explored as exhibited in Fig. 8. Compared with Zr-Ti-SBA-15, the XPS spectrum of Zr-Ti-SBA-15-C_0 presents a strong peak centered at 458.2 eV corresponding to the existence of large amounts of TiO_2. However, the presence of one component (Fig. 8a) of Ti 2p in the Zr-Ti-SBA-15 sample might indicate that practically all Ti atoms have been incorporated into the SBA-15 framework [36]. These results are also supported by XRD data of the samples.

4 Adsorption measurement of Zr-Ti-SBA-15

To unveil a potential adsorption activity, the obtained Zr-Ti-SBA-15 samples toward the organic dye from aqueous solution were tested in a batch experiment by choosing MB as the model organic dye. The effect of time, adsorbent dosage, pH and initial concentration of MB were investigated, as shown in Additional file 1: Figure S1. Obviously, the adsorption equilibrium time of MB on Zr-Ti-SBA-15 was established within 20 min in Additional file 1: Figure S1a, which according to previous work, this rapid adsorption at the initial stage is attributed to the large number of active sites on the adsorbent surface [37]. Furthermore, the increasing amount of adsorbent dosage is favorable for adsorption process, whereas the removal rate has no obvious change with the dosage increases (> 0.5 g L^{-1}).

The solution pH is an important parameter for the adsorption process. The zero charge of the Zr-Ti-SBA-15 sample is shown in the inset of Additional file 1: Figure S1c, and the pH_{pzc} is 5.6. As seen from Additional file 1: Figure S1c, the maximum adsorption capacity of the Zr-Ti-SBA-15 was observed at pH = 6, which is owing to the electrostatic interaction between the MB and the surface of Zr-Ti-SBA-15 samples [38]. From Additional file 1: Figure S1d, it is noted that the adsorption efficiency of MB is greater than that of high

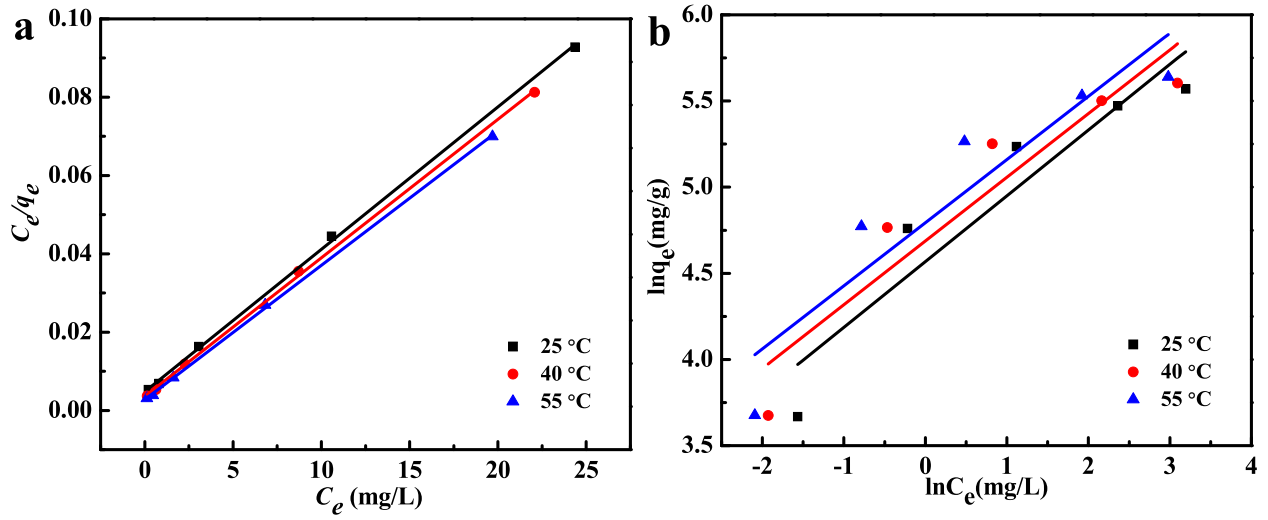

Fig. 10 Adsorption isotherm of MB on Zr-Ti-SBA-15 **a** Langmuir, **b** Freundlich

Table 4 Isothermal parameters for MB adsorption on Zr-Ti-SBA-15 composite

Temperature	Langmuir			Freundlich		
	b(L/mg)	q_m (mg/g)	R^2	1/n	k_f	R^2
25 °C	0.748	275.48	0.99931	0.381	96.36	0.84993
40 °C	0.983	282.49	0.99940	0.370	108.57	0.85349
55 °C	1.229	291.56	0.99959	0.366	120.74	0.82153

concentration of MB, which could be explained by the fact that the adsorption sites is gradually occupied with increase of initial concentration of MB.

4.1 Kinetic analysis

To further understand the adsorption mechanism of MB on the Zr-Ti-SBA-15 samples, two most commonly kinetic models, namely the pseudo-first-order (PFO) and pseudo-second-order (PSO) model, were applied here to fit the experimental data attained from batch experiments [39]. The corresponding linear equations are described as (1)–(2), consecutively.

$$t/q_t = 1/k_2 q^2{}_e + t/q_e \quad (1)$$

$$\log(q_e - q_t) = \log q_e - k_1 \times t/2.303 \quad (2)$$

Where q_t(mg g^{-1}) is the amount of adsorbate at time t; k_1(min^{-1}) is the rate constant of the PFO adsorption process; t is adsorption time; m (g L^{-1}) means adsorbent concentration; q_e (mg/g) is the equilibrium adsorbance of the adsorbent; k_2 [g $(mg \cdot min)^{-1}$] represents the rate constant of the PSO adsorption process.

The PFO and PSO plots are fitted by linear regression of the experimental data for MB on the mesoporous Zr-Ti-SBA-15 samples, as shown in Fig. 9a, b. Comparatively, it is found that the kinetic data could be best fitted into the PSO. The calculated parameters from kinetic models were presented in Table 3. Obviously, the correlation coefficient ($R^2 > 0.999$) values of the PSO is considerably higher than that of the PFO [40]. Meantime, the calculated equilibrium adsorbance (qe, cal) of the PSO is extremely close to the corresponding experimental equilibrium adsorbance (qe,exp). This indicates that, the adsorption behavior of MB on the Zr-Ti-SBA-15 samples takes place in consistence with PSO kinetic model, resulting from the chemical adsorption related to the valence forces by sharing or exchanging electrons between the MB and adsorbents [41].

4.2 Adsorption isotherms

As is known to all, the adsorption isotherm is an important isotherm to understand the interaction between adsorbent and adsorbate. Thus, Langmuir and Freundlich isotherms were fitted in our work to analyze the adsorption of MB on the as-prepared Zr-Ti-SBA-15 [39]. The equations are as follows:

$$C_e/q_e = 1/bq_m + C_e/q_m \quad (3)$$

$$\log q_e = \log k_f + 1/n \log C_e \quad (4)$$

Where q_e (mg/g) is the amount of dye adsorbed per unit; C_e(mg L^{-1}) means concentration at adsorption equilibrium; q_m (mg/g) is the maximum adsorption capacity; b (L mg^{-1}) is Langmuir constant; k_f is adsorption amount per unit concentration; *1/n* is generally between 0 and 1, and the size of the value indicates the stringency of the adsorption capacity.

Two adsorption isotherms plots were depicted in Fig. 10, and the related parameters of adsorption isotherms calculated from above mentioned equations are listed in Table 4. The results indicate that Langmuir model is more suitable to describe the adsorption behavior of MB on Zr-Ti-SBA-15, and the surface of Zr-Ti-SBA-15 is homogeneous with the adsorption mechanism of monolayer uptake [42]. As also seen in Table 4, the adsorption capacities of Zr-Ti-SBA-15 for

Table 5 Comparison of the maximum adsorption capacity of different adsorbents

Adsorbent	Adsorption capacity (q_m, mg/g)	Reference
FSAC	184.40	[38]
MS	111.65	[39]
AC- alginate beads	230	[40]
nitrogen and oxygen-doped porous carbon	100	[41]
GO / PEI(3D)aerogel	249.6	[42]
PPy / TiO_2	323.62	[43]
Zr-Ti-SBA-15	291.55	This study

Table 6 The values of thermodynamics parameters for MB adsorption on Zr-Ti-SBA-15

Temperature(K)	ΔG (kJ/mol)	ΔH (kJ/mol)	ΔS(J/mol·K)
298.15	−31.1	13.48	149.5
313.15	−33.4		
328.15	−35.6		

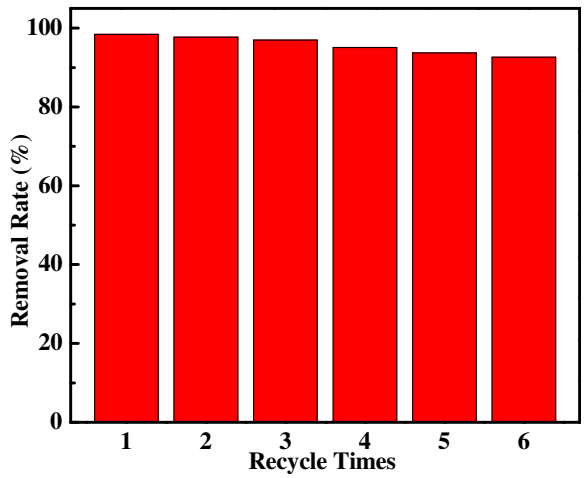

Fig. 11 Effect of recycle times on MB removal rate

MB are varied in the range of 275.5~291.6 mg/g. In comparison to some adsorbents for MB in previous literature, it can be stated that our findings are remarkably good (Table 5).

4.3 Thermodynamics analysis

To comprehend the effect of temperature on the adsorption of MB onto present Zr-Ti-SBA-15, Gibbs free energy ($\Delta G°$), enthalpy change ($\Delta H°$), entropy change ($\Delta S°$) were examined. The Langmuir isotherm was applied to calculate thermodynamics parameters [43]; the equation was given as follows:

$$\Delta G^\circ = -\mathrm{RTlnb} \tag{5}$$

$$\mathrm{lnb} = \frac{\Delta \mathrm{S}^\circ}{R} - \frac{\Delta \mathrm{H}^\circ}{RT} \tag{6}$$

Where b is the Langmuir equilibrium constant (L mol^{-1}); R represents the gas constant (8.314J (mol K)$^{-1}$).

The related thermodynamic parameters at various temperatures were given in Table 6. The negative values demonstrate the feasibility of the adsorption process and the spontaneous. Moreover, it is found that the value of $\Delta G°$ decreases when temperature increase, implying that adsorption of MB on Zr-Ti-SBA-15 is favored at higher temperature. The positive value of $\Delta H°$ demonstrates that the adsorption reaction is endothermic. Likewise, the value of $\Delta S°$ is positive, reflecting some structural change in MB and Zr-Ti-SBA-15 and the affinity for MB [44].

Table 7 The leaching data of Zr and Ti during desorption process

Metal elements	Metal released during desorption (mg/g)
Zr	0.000864
Ti	0.000196

4.4 Regeneration experiment of Zr-Ti-SBA-15

In practical application, regeneration and stability of products are of importance. The adsorption-desorption experiments of the Zr-Ti-SBA-15 were conducted, as given in Fig. 11. With consecutive adsorption-desorption process, the renewable Zr-Ti-SBA-15 also exhibits satisfactory adsorption rate with a value of 6.0%, which is slightly lower than that of initial samples after six cycles. To explore the reason for the reduction of adsorption ability for Zr-Ti-SBA-15, the filtrate after desorption was characterized by ICP. As shown in Table 7, the low concentration of Zr and Ti released into filtrate were detected, suggesting that the reduction of adsorption ability on Zr-Ti-SBA-15 is mainly caused by partial deletion of active site. In summary, the as-obtained Zr-Ti-SBA-15 materials with desirable reusability and recyclability possess highly efficient-stable adsorption activity for the removal of MB from mimic waste water.

5 Conclusion

Zr-Ti-SBA-15 with large specific surface area has been synthesized via a simple method. By using lactic acid as masking agent, Zr and Ti atoms were successfully incorporated homogenously into the SBA-15 framework, and no oxides particles were observed in Zr-Ti-SBA-15 samples, as demonstrated by all the characterizations. Meantime, MB adsorption capacity on as-prepared Zr-Ti-SBA-15 is measured to be much higher (291.6 mg/g) and faster (20 min) than that of other adsorbents reported in the literatures, exhibiting the excellent adsorption performance of Zr-Ti-SBA-15. Additionally, such materials have also shown such fantastic stability that it could be reused for 6 times without obvious variation in adsorption activity. Based on the results obtained, the adsorption mechanism of MB on Zr-Ti-SBA-15 could be appropriately described by the adsorption isotherm of Langmuir and pseudo-second-order kinetic model, demonstrating the MB adsorption on Zr-Ti-SBA-15 is monolayer uptake and chemical adsorption, respectively. Furthermore, thermodynamic analysis indicates that its adsorption reaction is an endothermic and spontaneous process. This work suggests that the as-prepared Zr-Ti-SBA-15 may serve as promising dual functional materials for environmental pollution cleanup.

6 Additional file

Additional file 1: Figure S1. Effects of contact time, adsorbent dosage, solution pH and initial concentration of MB on MB adsorption ability. (DOCX 126 kb)

Acknowledgements
This work was funded by National Natural Science Foundation of China grant number 51403210 and the Innovation Foundation of Graduate Student in Shaanxi University of Science and Technology and also supported by the Center for High Performance Computing of Northwestern Polytechnical University and the Youth Innovation Team of Shaanxi Universities and the New Style Think Tank of Shaanxi Universities, China.

Authors' contributions
TQ and JZ conceived and designed the study. YX and JZ performed the experiments and analyzed the experiments data. TQ, YX and JZ reviewed and edited the manuscript. All authors read and approved the manuscript.

Funding
This work was funded by National Natural Science Foundation of China grant number 51403210.

Availability of data and materials
All data generated or analyzed during this study are included in this published article. The authors declare that the data in this article is reliable.

Competing interests
The authors declare that they have no competing interests.

Received: 22 January 2019 Accepted: 20 May 2019
Published: 22 July 2019

References

1. Ramalingam B, et al. Facile Synthesis of Silver Nanoparticles Decorated Magnetic-Chitosan Microsphere for Efficient Removal of Dyes and Microbial Contaminants. ACS Sustain Chen Eng. 2015;3:2291–2302. https://doi.org/10.1021/acssuschemeng.5b00577.
2. Acosta-Silvaa YJ, et al. Methylene blue photodegradation over titania-decorated SBA-15. Appl Catal B Environ. 2011;110:108–17. https://doi.org/10.1016/j.apcatb.2011.08.032.
3. Peng N, et al. Superabsorbent cellulose–clay nanocomposite hydrogels for highly efficient removal of dye in water. ACS Sustain Chem Eng. 2016;4:7217–24. https://doi.org/10.1021/acssuschemeng.6b02178.
4. He C, Hu XJ. Anionic dye adsorption on chemically modified ordered mesoporous carbons. Ind Eng Chem Res. 2011;50:14070–83. https://doi.org/10.1021/ie201469p.
5. Parker HL, et al. The importance of being porous: polysaccharide-derived mesoporous materials for use in dye adsorption. RSC Adv. 2012;2:8992–7. https://doi.org/10.1039/C2RA21367B.
6. Li YL, et al. Synthesis of magnetic lignin-based hollow microspheres: A highly adsorptive and reusable adsorbent derived from renewable resources. ACS Sustain Chem Eng. 2016;4:5523–32. https://doi.org/10.1021/acssuschemeng.6b01244.
7. Ahmad R, Mondal PK, Usmani SQ. Hybrid UASFB-aerobic bioreactor for biodegradation of acid yellow-36 in wastewater. Bioresour Technol. 2010;101:3787–90. https://doi.org/10.1016/j.biortech.2009.12.116.
8. Xie YJ, et al. Highly regenerable mussel-inspired Fe_3O_4@ polydopamine-Ag core–shell microspheres as catalyst and adsorbent for methylene blue removal. ACS Appl Mater Inter. 2014;6:8845–52. https://doi.org/10.1021/am501632f.
9. Ahmed MA, Brick AA, Mohamed AA. An efficient adsorption of indigo carmine dye from aqueous solution on mesoporous Mg/Fe layered double hydroxide nanoparticles prepared by controlled sol-gel route. Chemosphere. 2017;174:280–8. https://doi.org/10.1016/j.chemosphere.2017.01.147.
10. Zhang ZQ, et al. Pd and Pt nanoparticles supported on the mesoporous silica molecular sieve SBA-15 with enhanced activity and stability in catalytic bromate reduction. Chem Eng J. 2018;344:114–23. https://doi.org/10.1016/j.cej.2018.03.056.
11. Atakan A, Erdtman E, Mäkie P, Ojamäe L, Odén M. Time evolution of the CO_2 hydrogenation to fuels over Cu-Zr-SBA-15 catalysts. J Catal. 2018;362:55–64. https://doi.org/10.1016/j.jcat.2018.03.023.
12. Ganiyu SA, Alhooshani K, Ali SA. Single-pot synthesis of Ti-SBA-15-NiMo hydrodesulfurization catalysts: role of calcination temperature on dispersion and activity. Appl Catal B Environ. 2017;203:428–41. https://doi.org/10.1016/j.apcatb.2016.10.052.
13. Huye PT, Nam LTH, Vinh TQ, Martínez C, Parvulescu VI. ZSM-5/SBA-15 versus Al-SBA-15 as supports for the hydrocracking/hydroisomerization of alkanes. Catal Today. 2018;306:121–7. https://doi.org/10.1016/j.cattod.2017.03.040.
14. Cai C, Zhang ZY, Zhang H. Electro-assisted heterogeneous activation of persulfate by Fe/SBA-15 for the degradation of Orange II. J Hazard Mater. 2016;313:209–18. https://doi.org/10.1016/j.jhazmat.2016.04.007.
15. Jung WY, Lee GD, Park SS, Lim KT, Hong SS. Photocatalytic decomposition of methylene blue over yttrium ion doped Ti-SBA-15 catalysts. Catal Today. 2011;164:395–8. https://doi.org/10.1016/j.cattod.2010.11.047.
16. Das SK, Bhunia MK, Bhaumik A. Highly ordered Ti-SBA-15: efficient H2adsorbent and photocatalyst for eco-toxic dye degradation. J Solid State Chem. 2010;183:1326–33. https://doi.org/10.1016/j.jssc.2010.04.015.
17. Visuvamithiran P, Shanthi K, Palanichamya M, Murugesan V. Direct synthesis of Mn-Ti-SBA-15 catalyst for the oxidation of ethylbenzene. Catal Sci Technol. 2013;3:2340–8. https://doi.org/10.1039/c3cy00306j.
18. Cheng M, et al. A novel and simple strategy for the direct synthesis bimetallic mesoporous materials Zr–La-SBA-15. Mater Lett. 2014;128:15–8. https://doi.org/10.1016/j.matlet.2014.04.015.
19. Subbaramaiah V, Srivastava VC, Mall ID. Optimization of reaction parameters and kinetic modeling of catalytic wet peroxidation of picoline by Cu/SBA-15. Ind Eng Chem Res. 2013;52:9021–9. https://doi.org/10.1021/ie400124d.
20. Yang LL, Wang B, Lai SF, Jiang CW, Zhong H. Enhancing photocatalytic degradation of phenol through nitrogen- and nitrogen/fluorine-codoped Ti-SBA-15. RSC Adv. 2015;5:53299–305. https://doi.org/10.1039/c5ra09922f.
21. Zhang WJ, Wang H, Han JY, Song ZQ. Multifunctional mesoporous materials with acid–base frameworks and ordered channels filled with ionic liquid: synthesis, characterization and catalytic performance of Ti–Zr-SBA-15-IL. Appl Surf Sci. 2012;258:6158–68. https://doi.org/10.1016/j.apsusc.2012.03.034.
22. Mouli KC, Mohanty S, Hu YF, Dalai A, Adjaye J. Effect of hetero atom on dispersion of NiMo phase on M-SBA-15 (M = Zr, Ti, Ti-Zr). Catal Today. 2013;207:133–44. https://doi.org/10.1016/j.cattod.2012.07.010.
23. Qiang TT, Zhao J, Li J. Direct synthesis of homogeneous Zr-doped SBA-15 mesoporous silica via masking zirconium sulfate. Micropor Mesopor Mater. 2018;257:162–74. https://doi.org/10.1016/j.micromeso.2017.08.041.
24. Chen SY, Mochizuki T, Abe Y, Toba M, Yoshimura Y. Ti-incorporated SBA-15 mesoporous silica as an efficient and robust Lewis solid acid catalyst for the production of high-quality biodiesel fuels. Appl Cataly B Environ. 2014;148:344–56. https://doi.org/10.1016/j.apcatb.2013.11.009.
25. Sun JY, et al. Enhanced catalytic hydrogenation reduction of bromate on Pd catalyst supported on CeO_2 modified SBA-15 prepared by strong electrostatic adsorption. Appl Catal B Environ. 2018;229:32–40. https://doi.org/10.1016/j.apcatb.2018.02.009.
26. Wróblewska A, et al. Alpha-pinene isomerization over Ti-SBA-15 catalysts obtained by the direct method: the influence of titanium content, temperature, catalyst amount and reaction time. Micropor Mesopor Mater. 2018;258:72–82. https://doi.org/10.1016/j.micromeso.2017.09.007.
27. Lee YY, Jung HS, Kim JM, Kang YT. Photocatalytic CO_2 conversion on highly ordered mesoporous materials: comparisons of metal oxides and compound semiconductors. Appl Catal B Environ. 2018;224:594–601. https://doi.org/10.1016/j.apcatb.2017.10.068.
28. Barczak M, Wierzbicka M, Borowski P. Sorption of diclofenac onto functionalized mesoporous silicas: experimental and theoretical investigations. Micropor Mesopor Mater. 2018;264:254–64. https://doi.org/10.1016/j.micromeso.2018.01.013.
29. Gao JS, et al. 3D mesoporous $CuFe_2O_4$ as a catalyst for photo-Fenton removal of sulfonamide antibiotics at near neutral pH. J Colloid Inter Sci. 2018;524:409–16. https://doi.org/10.1016/j.jcis.2018.03.112.
30. Guo J, Sotto A, Martín A, Kim J. Preparation and characterization of polyethersulfone mixed matrix membranes embedded with Ti-or Zr-incorporated SBA-15 materials. J Ind Eng Chem. 2017;45:257–65. https://doi.org/10.1016/j.jiec.2016.09.033.
31. Zhao D, et al. Triblock copolymer syntheses of mesoporous silica with periodic 50 to 300 angstrom pores. Science. 1998;279:548–52. https://doi.org/10.1126/science.279.5350.548.
32. Devi P, Das U, Dalai AK. Production of glycerol carbonate using a novel Ti-SBA-15 catalyst. Chem Eng J. 2018;346:477–88. https://doi.org/10.1016/j.cej.2018.04.030.
33. Meng YY, An QD, Xiao ZY, Zhai SR, Shi Z. Pd NPs supported on N-doped carbon layer coated Zr-SBA-15 for efficient heterogeneous catalysis

reactions. Micropor Mesopor Mater. 2018;266:64–74. https://doi.org/10.1016/j.micromeso.2018.02.042.
34. Thunyaratchatanon C, et al. Synthesis and characterization of Zr incorporation into highly ordered mesostructured SBA-15 material and its performance for CO_2 adsorption. Micropor Mesopor Mater. 2017;253:18–28. https://doi.org/10.1016/j.micromeso.2017.06.015.
35. Tang YQ, et al. Zirconia functionalized SBA-15 as effective adsorbent for phosphate removal. Micropor Mesopor Mater. 2012;155:192–200. https://doi.org/10.1016/j.micromeso.2012.01.020.
36. Santacesaria E, Cozzolino M, Serio MD, Venezia AM, Tesser R. Vanadium based catalysts prepared by grafting: preparation, properties and performances in the ODH of butane. Appl Catal A Gen. 2004;270:177–92. https://doi.org/10.1016/j.apcata.2004.05.003.
37. Tang L, et al. Synergistic effect of iron doped ordered mesoporous carbon on adsorption-coupled reduction of hexavalent chromium and the relative mechanism study. Chem Eng J. 2014;239:114–22. https://doi.org/10.1016/j.cej.2013.10.104.
38. Tao J, et al. Hybrid mesoporous silica based on hyperbranch-substrate nanonetwork as highly efficient adsorbent for water treatment. ACS Sustain Chem Eng. 2016;4:60–8. https://doi.org/10.1021/acssuschemeng.5b00652.
39. Li JJ, Zhang Q, Feng JT, Yan W. Synthesis of PPy-modified TiO_2 composite in H_2SO_4 solution and its novel adsorption characteristics for organic dyes. Chem Eng J. 2013;225:766–75. https://doi.org/10.1016/j.cej.2013.03.011.
40. García-Martínez JC, et al. Selective adsorption of nitrogen compounds using silica-based mesoporous materials as a pretreatment for deep hydrodesulfurization. Catal Today. 2018;305:40–8. https://doi.org/10.1016/j.cattod.2017.10.037.
41. Sun PP, et al. Hydrothermal synthesis of mesoporous $Mg_3Si_2O_5(OH)_4$ microspheres as high-performance adsorbents for dye removal. Chem Eng J. 2018;334:377–88. https://doi.org/10.1016/j.cej.2017.09.120.
42. Zhang M, Yao Q, Lu C, Li Z, Wang W. Layered double hydroxide–carbon dot composite: high-performance adsorbent for removal of anionic organic dye. ACS Appl Mater Inter. 2014;6:20225–33. https://doi.org/10.1021/am505765e.
43. Yao Y, Xu F, Chen M, Xu Z, Zhu Z. Adsorption behavior of methylene blue on carbon nanotubes. Bioresour Technol. 2010;101:3040–6. https://doi.org/10.1016/j.biortech.2009.12.042.
44. Huang Q, et al. Enhanced removal capability of kaolin toward methylene blue by mussel-inspired functionalization. J Mater Sci. 2016;51:8116–30. https://doi.org/10.1007/s10853-016-0082-6.

Publisher's Note